Mechanics Research Communications 96 (2019) 7–18

Contents lists available at ScienceDirect

Mechanics Research Communications

journal homepage: www.elsevier.com/locate/mechrescom

Modeling of fiber-reinforced polymeric gels

Nikola Bosnjak[a], Shuolun Wang[b], Daehoon Han[c], Howon Lee[c], Shawn A. Chester[a,*]

[a] Mechanical Engineering, New Jersey Institute of Technology, Newark, NJ 07102, USA
[b] Department of Mechanical and Industrial Engineering, University of Illinois at Chicago, Chicago, IL 60607, USA
[c] Department of Mechanical and Aerospace Engineering, Rutgers, The State University of New Jersey, Piscataway, NJ 08854, USA

ARTICLE INFO

Article history:
Received 27 December 2018
Accepted 5 February 2019
Available online 7 February 2019

Keywords:
Gels
Polymeric materials
Anisotropic materials
Diffusion
Finite elements

ABSTRACT

When a polymer network is exposed to a suitable solvent, the migration of solvent molecules into the network will cause volumetric deformation, known as swelling, but more importantly forms a mixture that is known as a polymeric gel. Despite numerous potential applications, many aspects of the coupled diffusion-deformation behavior in polymeric gels have not yet been thoroughly investigated. Here, we focus our attention on the coupled deformation-diffusion response of fiber-reinforced polymeric gels. The presence of embedded fibers in a swellable polymer matrix leads to anisotropy in the overall behavior. In order to capture this response, we have developed a constitutive model for fiber-reinforced polymeric gels, that explicitly takes into account anisotropy in both the mechanical and diffusive behavior. The constitutive model is implemented as user element subroutine (UEL) in the commercial finite element software package Abaqus/Standard. Numerical simulations are performed to show the behavior of the model, and qualitative comparisons are made to experiments of a soft robotic gripper.

1. Introduction

Mixing a polymeric network with a suitable solvent will cause the network to expand, allowing for solvent diffusion and volumetric deformation, commonly referred to as swelling. A polymer material in this mixed and swollen state is known as a polymeric gel.

Gels are ubiquitous, they are used in many applications from packers in the oil industry [6,34] to drug delivery systems [10]. Due to the similarity between polymeric gels and biological tissues, polymeric gels are widely used in tissue engineering as scaffolds [35], injectable cartilage and tissue formations [37]. An important distinction between biological tissues and much of the previous literature on the mechanics of polymeric gels is that most biological tissues contain fibers. The existence of these fibers embedded in the material, causes the properties to be significantly different along the fiber direction [15,16,42,46,50]. In other words, the presence of embedded fibers imposes pronounced anisotropy in the response of these materials.

Also, many polymers respond to environmental stimuli such as temperature, electric and magnetic fields, pH, and more [22,23,26,27,33,36,47,52]. The responsiveness of polymeric gels to environmental stimuli has been widely employed in soft robotics [44,49]. The applications of soft robots are vast [32], the more exotic ones include morphing airfoils, rotary actuators, and grippers [7,24,51]. Newly designed polymeric gels are being developed to enhance the performance of these systems [53]. Further, the flexibility of soft robots and their similarity to biological systems are utilized in bio-hybrid robotics [9]. The fast emerging development of gel-based soft robots makes modeling of this class of materials an important task for simulating their operation.

The early research of Tanaka and Fillmore [48] is commonly considered the starting point of modern day research on polymeric gels. In recent years, there have been many notable attempts to formulate theories capable of capturing multiphysics behavior of isotropic gels [cf., e.g., [5,12,14,18–20,30,38,39]]. In the literature, one also finds a vast number of constitutive models for capturing anisotropic behavior of fiber-reinforced polymers [cf., e.g., [2,8,29,43]]. However, there are only a few notable attempts to include influence of embedded fibers on behavior of polymeric gels in recent years [40,41,45].

The objective of this work is to develop a continuum level coupled deformation-diffusion constitutive model for fiber-reinforced polymeric gels. The novelty of the model is that it builds upon previous work by taking into account the mechanical influence of fibers, as well as the anisotropic diffusion they may impart. The behavior of the dry polymer matrix is modeled using a non-Gaussian statistical mechanics based model that takes limited chain extensibility into account. In addition to the behavior of dry polymer matrix, we include the contribution of embedded fibers with a volume fraction and modulus. The mechanical behavior of

---

[*] Corresponding author.
E-mail address: shawn.a.chester@njit.edu (S.A. Chester).

https://doi.org/10.1016/j.mechrescom.2019.02.002
0093-6413/

polymer network is coupled with the diffusion of solvent by implementing Flory-Huggins model for mixing free energy between polymer network and solvent. We assume the embedded fibers do not imbibe solvent, and accordingly there is no mixing between the fiber and solvent. Further, we numerically implemented our multiphysics constitutive model in commercially available finite element software package Abaqus/Standard [1] by writing a user element subroutine (UEL). The numerical implementation allows for the behavior and capabilities of the model to be presented through boundary value problems. Lastly, to show the usefulness of the model and it's implementation, a qualitative comparison is made between the model and an experimentally realized soft robotic gripper.

The remainder of this paper is organized as follows. Section 2 summarizes the continuum level framework, in Section 3 we presented the overview of thermodynamics of the system, in Section 4 we provide basic constitutive equations and in Section 5 we show the specialization of free energy for fiber-reinforced polymeric gels. Section 6 shows the usefulness of our constitutive model and numerical simulation procedure. In Section 7 we show a comparison between the operation of our diffusion activated soft gripper and its numerical simulation. We finish with some concluding remarks in Section 8. In an Appendix, Section 9 we present the governing equations and the numerical solution procedure using finite elements required for numerical implementation.

2. Continuum framework

We begin by summarizing the governing continuum level equations for coupled solvent diffusion and large deformation of soft polymeric gels. For further details, the reader is referred to our previous work in the literature [cf., e.g., 14, and references therein].

2.1. Kinematics

Consider a *dry* body $\mathcal{B}_\mathrm{R}$ identified with the region of space it occupies in a fixed reference configuration, and denote by $\mathbf{x}_\mathrm{R}$ an arbitrary material point of $\mathcal{B}_\mathrm{R}$. The dry referential body $\mathcal{B}_\mathrm{R}$ then undergoes a motion $\mathbf{x} = \boldsymbol{\chi}(\mathbf{x}_\mathrm{R}, t)$ to the deformed body $\mathcal{B}_t$ with deformation gradient given by[1]

$$\mathbf{F} = \nabla\boldsymbol{\chi}, \text{ such that } J = \det\mathbf{F} > 0. \tag{1}$$

The right and left Cauchy–Green deformation tensors are given by $\mathbf{C} = \mathbf{F}^\top\mathbf{F}$ and $\mathbf{B} = \mathbf{F}\mathbf{F}^\top$, respectively. Additionally, to model the fibers, we assume γ different fiber orientations may be present in the dry reference body, denoted by the term *family*. Each fiber family is characterized by a direction $\mathbf{a}_\mathrm{R}^{(\gamma)}$ (a unit vector), and volume fraction $f_\mathrm{R}^{(\gamma)}$ in $\mathcal{B}_\mathrm{R}$. *At the outset, we assume that the fibers do not absorb any solvent and remain dry, and are perfectly bonded to the polymer matrix*. Following the approach in Holzapfel [28], a pseudo-invariant is introduced for each family of fibers, which as previously noted has been used to model the anisotropic response of fiber-reinforced soft materials [40,41,50]. Specifically, we use the pseudo-invariant

$$I_4^{(\gamma)} = \mathbf{a}_\mathrm{R}^{(\gamma)} \cdot \mathbf{C}\mathbf{a}_\mathrm{R}^{(\gamma)} = \left(\lambda^{(\gamma)}\right)^2, \tag{2}$$

where $\lambda^{(\gamma)}$ has the physical interpretation of the stretch along the fiber family direction $\mathbf{a}_\mathrm{R}^{(\gamma)}$ for each γ.

The theory is based upon a multiplicative decomposition

$$\mathbf{F} = \mathbf{F}^m\mathbf{F}^s, \text{ with } \mathbf{F}^s = \lambda^s\mathbf{1}, \tag{3}$$

of the deformation gradient $\mathbf{F}$ into a mechanical part, $\mathbf{F}^m$, and a swelling part $\mathbf{F}^s$, with λ^s the swelling stretch. Further, this allows us to rewrite the right Cauchy–Green tensor in the form

$$\mathbf{C} = (\mathbf{F}^m\mathbf{F}^s)^\top(\mathbf{F}^m\mathbf{F}^s) = (\lambda^s)^2\mathbf{F}^{m\top}\mathbf{F}^m = (\lambda^s)^2\mathbf{C}^m. \tag{4}$$

Based on (3), the relative volume change is given by

$$J = \det\mathbf{F} = \det(\mathbf{F}^m\mathbf{F}^s) = J^mJ^s, \text{ with } \det\mathbf{F}^m = J^m > 0, \text{ and } \det\mathbf{F}^s = J^s > 0, \tag{5}$$

where J^m is the volume change due to mechanical effects, and J^s the volume change due to swelling. As is typical in the literature [12,30] we assume the volume change due to swelling is given by

$$J^s = 1 + \Omega c_\mathrm{R}, \quad \text{and therefore} \quad \lambda^s = (1 + \Omega c_\mathrm{R})^{1/3}. \tag{6}$$

Here c_R represents the *solvent content* measured in moles of solvent per unit reference volume of the dry polymer, and Ω the volume of a mole of solvent.

Further, using (1) and (3), we write velocity gradient

$$\mathbf{L} = \dot{\mathbf{F}}\mathbf{F}^{-1} = \mathbf{L}^m + \mathbf{F}^m\mathbf{L}^s\mathbf{F}^{m-1} \tag{7}$$

with $\mathbf{L}^m$ and $\mathbf{L}^s$, mechanical and swelling part, respectively, given by

$$\mathbf{L}^m = \dot{\mathbf{F}}^m\mathbf{F}^{m-1} \quad \text{and} \quad \mathbf{L}^s = \dot{\mathbf{F}}^s\mathbf{F}^{s-1}. \tag{8}$$

Next, we define the mechanical and swelling stretching and spin tensors

$$\begin{aligned} \mathbf{D}^m &= \operatorname{sym}\mathbf{L}^m, \quad \mathbf{W}^m = \operatorname{skw}\mathbf{L}^m, \\ \mathbf{D}^s &= \operatorname{sym}\mathbf{L}^s, \quad \mathbf{W}^s = \operatorname{skw}\mathbf{L}^s, \end{aligned} \tag{9}$$

so that $\mathbf{L}^m = \mathbf{D}^m + \mathbf{W}^m$ and $\mathbf{L}^s = \mathbf{D}^s + \mathbf{W}^s$.

Recalling (3), (8) and (9) we obtain

$$\mathbf{D}^s = \left(\dot{\lambda}^s\lambda^{s-1}\right)\mathbf{1} \quad \text{and} \quad \mathbf{W}^s = \mathbf{0}, \tag{10}$$

and since

$$\dot{J}^s = J^s\operatorname{tr}\mathbf{D}^s, \tag{11}$$

we may write

$$\mathbf{D}^s = \frac{1}{3}\left(\dot{J}^sJ^{s-1}\right)\mathbf{1}. \tag{12}$$

2.2. Balance of forces and moments

Neglecting inertial effects, the balance of forces and moments in the referential body $\mathcal{B}_\mathrm{R}$ are expressed as

$$\operatorname{div}\mathbf{T}_\mathrm{R} + \mathbf{b}_\mathrm{R} = \mathbf{0} \quad \text{and} \quad \mathbf{T}_\mathrm{R}\mathbf{F}^\top = \mathbf{F}\mathbf{T}_\mathrm{R}^\top \tag{13}$$

respectively, where $\mathbf{T}_\mathrm{R}$ is first Piola stress and $\mathbf{b}_\mathrm{R}$ is an external body force per unit referential volume. The boundary of the referential body has outward unit normal $\mathbf{n}_\mathrm{R}$. The surface traction on an element of the referential surface is given by $\mathbf{t}_\mathrm{R} = \mathbf{T}_\mathrm{R}\mathbf{n}_\mathrm{R}$. As common in continuum mechanics, the Piola stress is related to Cauchy stress $\mathbf{T}$ in the deformed body by

$$\mathbf{T}_\mathrm{R} = J\mathbf{T}\mathbf{F}^{-\top}, \quad \text{therefore,} \quad \mathbf{T} = J^{-1}\mathbf{T}_\mathrm{R}\mathbf{F}^\top. \tag{14}$$

In the current configuration the balance of forces and moments is given in the deformed body $\mathcal{B}_t$ by

$$\operatorname{div}\mathbf{T} + \mathbf{b} = \mathbf{0} \quad \text{and} \quad \mathbf{T} = \mathbf{T}^\top, \tag{15}$$

where $\mathbf{b}$ is the external body force per unit current volume. Lastly, the surface traction on the boundary of deformed body with outward unit normal $\mathbf{n}$ is $\mathbf{t} = \mathbf{T}\mathbf{n}$.

---

[1] The symbols ∇, Div and Curl denote the gradient, divergence and curl with respect to the material point $\mathbf{x}_\mathrm{R}$ in the reference configuration; grad, div and curl denote these operators with respect to the point $\mathbf{x} = \boldsymbol{\chi}(\mathbf{x}_\mathrm{R}, t)$ in the deformed configuration.

2.3. Balance of solvent content

We assume that the intake and outflow of solvent does not involve any chemical reactions. Therefore, the balance of solvent content in the referential and current configurations takes the form

$$\dot{c}_{\mathrm{R}} = -\mathrm{div}\ \mathbf{j}_{\mathrm{R}} \quad \text{and} \quad \dot{c}_{\mathrm{R}} = -J\mathrm{div}\ \mathbf{j}, \tag{16}$$

where $\mathbf{j}_{\mathrm{R}}$ and $\mathbf{j}$ are the fluid flux in referential and current configuration, respectively.

Defining the *polymer volume fraction*

$$\phi \overset{\mathrm{def}}{=} \frac{1}{1+\Omega c_{\mathrm{R}}} = (\lambda^s)^{-3} = (J^s)^{-1} \tag{17}$$

which lies in the range $0<\phi<1$, the balance of solvent content (16) may be rewritten in the referential and current forms

$$\frac{\dot{\phi}}{\Omega\phi^2} - \mathrm{div}\ \mathbf{j}_{\mathrm{R}} = 0 \quad \text{and} \quad \frac{\dot{\phi}}{J\Omega\phi^2} - \mathrm{div}\ \mathbf{j} = 0. \tag{18}$$

Here $\phi \to 1$ is simply a dry polymer, while $\phi<1$ is a locally swollen state. Lastly, the surface flux into an element of the referential and current surface is given by $j_{\mathrm{R}} = -\mathbf{j}_{\mathrm{R}} \cdot \mathbf{n}_{\mathrm{R}}$ and $j = -\mathbf{j} \cdot \mathbf{n}$, respectively.

3. Thermodynamics

A complete thermodynamic derivation of a model for polymeric gels is thoroughly discussed in the earlier research published by our group. For more details regarding thermodynamics, the reader is referred to Chester and co-workers [11–13].

Let the body $\mathcal{B}_{\mathrm{R}}$ contain an arbitrary part $\mathcal{P}_{\mathrm{R}}$. Under isothermal conditions, the first two laws of thermodynamics may be combined into a single free energy imbalance. The free energy imbalance requires that the temporal increase in free energy in any part be less than or equal to the power expended plus that which is brought into that part from fluid transport. Specifically the free energy imbalance takes the form

$$\overline{\int_{\mathcal{P}_{\mathrm{R}}} \psi_{\mathrm{R}} dv_{\mathrm{R}}}^{\,\boldsymbol{\cdot}} \le \int_{\partial\mathcal{P}_{\mathrm{R}}} \mathbf{T}_{\mathrm{R}}\mathbf{n}_{\mathrm{R}} \cdot \dot{\boldsymbol{\chi}} da_{\mathrm{R}} + \int_{\mathcal{P}_{\mathrm{R}}} \mathbf{b}_{\mathrm{R}} \cdot \dot{\boldsymbol{\chi}} dv_{\mathrm{R}} - \int_{\partial\mathcal{P}_{\mathrm{R}}} \mu \mathbf{j}_{\mathrm{R}} \cdot \mathbf{n}_{\mathrm{R}} da_{\mathrm{R}}, \tag{19}$$

with μ the chemical potential of the solvent. Applying the divergence theorem to the terms in (19), we obtain

$$\int_{\mathcal{P}_{\mathrm{R}}} \Big(\dot{\psi}_{\mathrm{R}} - (\mathrm{div}\ \mathbf{T}_{\mathrm{R}} + \mathbf{b}_{\mathrm{R}}) \cdot \dot{\chi} - \mathbf{T}_{\mathrm{R}} : \dot{\mathbf{F}} + \mu \mathrm{div}\ \mathbf{j}_{\mathrm{R}} + \mathbf{j}_{\mathrm{R}} \cdot \nabla\mu\Big) dv_{\mathrm{R}} \le 0. \tag{20}$$

Using (13) and (16), since (20) must hold for every part $\mathcal{P}_{\mathrm{R}}$, we write

$$\dot{\psi}_{\mathrm{R}} - \mathbf{T}_{\mathrm{R}} : \dot{\mathbf{F}} - \mu\dot{c}_{\mathrm{R}} + \mathbf{j}_{\mathrm{R}} \cdot \nabla\mu \le 0. \tag{21}$$

Recalling (3) and (8), we decompose the stress power

$$\mathbf{T}_{\mathrm{R}} : \dot{\mathbf{F}} = \Big(J\mathbf{T}\mathbf{F}^{m-\top}\Big) : \dot{\mathbf{F}}^m + \Big(J\mathbf{F}^{m\,\top}\mathbf{T}\mathbf{F}^{m-\top}\Big) : \mathbf{L}^s. \tag{22}$$

Here, we introduce two new stress measures

$$\mathbf{S}^m \overset{\mathrm{def}}{=} J\mathbf{T}\mathbf{F}^{m-\top} \quad \text{and} \quad \mathbf{M}^m \overset{\mathrm{def}}{=} J\mathbf{F}^{m\,\top}\mathbf{T}\mathbf{F}^{m-\top}, \tag{23}$$

as a mechanical Piola stress and Mandell stress, respectively. Further, using (23), we can write (22) in the form

$$\mathbf{T}_{\mathrm{R}} : \dot{\mathbf{F}} = \mathbf{S}^m : \dot{\mathbf{F}}^m + \mathbf{M}^m : \mathbf{L}^s \tag{24}$$

In addition, we introduce mechanical second Piola stress

$$\mathbf{T}^m = J\mathbf{F}^{m-1}\mathbf{T}\mathbf{F}^{m-\top} \tag{25}$$

and since the rate of change of mechanical right Cauchy–Green tensor is $\dot{\mathbf{C}}^m = \mathbf{F}^{m\,\top}\dot{\mathbf{F}}^m + \dot{\mathbf{F}}^{m\,\top}\mathbf{F}^m$, we can write

$$\mathbf{T}^m : \dot{\mathbf{C}}^m = 2(\mathbf{F}^m\mathbf{T}^m) : \dot{\mathbf{F}}^m = 2\mathbf{S}^m : \dot{\mathbf{F}}^m. \tag{26}$$

Employing (10) and (12) we can write the stress-power (22) in the form

$$\mathbf{T}_{\mathrm{R}} : \dot{\mathbf{F}} = \frac{1}{2}\mathbf{T}^m : \dot{\mathbf{C}}^m - \bar{p}\dot{J}^s, \tag{27}$$

where we have defined the mean normal pressure, $\bar{p}$, as $\bar{p} \overset{\mathrm{def}}{=} -\frac{1}{3}J^m \mathrm{tr}\ \mathbf{T}$.

Applying the kinematical constraint between c_{R} and J^s given by (6), in (19), and using (27), we obtain the free energy imbalance in the form

$$\dot{\psi}_{\mathrm{R}} - \frac{1}{2}\mathbf{T}^m : \dot{\mathbf{C}}^m - \mu_{\mathrm{act}}\dot{c}_{\mathrm{R}} + \mathbf{j}_{\mathrm{R}} \cdot \nabla\mu \le 0, \tag{28}$$

where the active chemical potential is defined as $\mu_{\mathrm{act}} \overset{\mathrm{def}}{=} \mu - \bar{p}\Omega$.

4. Basic constitutive equations

Based on (28), and considering frame indifference, the basic constitutive equations are

$$\left.\begin{array}{ll} \psi_{\mathrm{R}} & = \bar{\psi}_{\mathrm{R}}(\mathbf{C}^m, c_{\mathrm{R}}) \\ \mathbf{T}^m & = \bar{\mathbf{T}}^m(\mathbf{C}^m, c_{\mathrm{R}}) \\ \mu_{act} & = \bar{\mu}_{act}(\mathbf{C}^m, c_{\mathrm{R}}) \end{array}\right\} \tag{29}$$

along with a Darcy-type relation for the spatial solvent flux

$$\mathbf{j} = -\bar{\mathbf{M}}(\mathbf{C}^m, c_{\mathrm{R}})\mathrm{grad}\ \mu, \tag{30}$$

where $\bar{\mathbf{M}}(\mathbf{C}^m, c_{\mathrm{R}})$ is the mobility tensor. Here, to account for any anisotropy due to the embedded fibers, or other sources of anisotropy, the mobility retains it's tensorial characteristic, and not simplified to a scalar in this work. Pushed back to the reference body, using the standard relations $\mathbf{j}_{\mathrm{R}} = J\mathbf{F}^{-1}\mathbf{j}$ and $\nabla\mu = \mathbf{F}^{\top}\mathrm{grad}\ \mu$, we may rewrite (30) in the referential form

$$\mathbf{j}_{\mathrm{R}} = -J\mathbf{F}^{-1}\bar{\mathbf{M}}(\mathbf{C}^m, c_{\mathrm{R}})\mathbf{F}^{-\top}\nabla\mu. \tag{31}$$

Sufficient conditions to satisfy (28) using (29) yield relations for the Cauchy stress

$$\mathbf{T} = J^{-1}\left[2\mathbf{F}^m \frac{\partial\bar{\psi}_{\mathrm{R}}(\mathbf{C}^m, c_{\mathrm{R}})}{\partial\mathbf{C}^m}\mathbf{F}^{m\,\top}\right], \tag{32}$$

and the chemical potential

$$\mu = \frac{\partial\bar{\psi}_{\mathrm{R}}(\mathbf{C}^m, c_{\mathrm{R}})}{\partial c_{\mathrm{R}}} + \Omega\bar{p}. \tag{33}$$

We further note that to satisfy the thermodynamic imbalance in (28), the mobility tensor $\bar{\mathbf{M}}(\mathbf{C}^m, c_{\mathrm{R}})$ has to be positive definite in the presence of solvent and whenever $\nabla\mu \neq \mathbf{0}$.

5. Specialized constitutive equations

5.1. Free energy

For ease of notation, and following the approach used to include the fiber volume fraction in Pan and Zhong [45], we define

$$f_{\mathrm{R}} = \sum_{\gamma} f_{\mathrm{R}}^{(\gamma)} \tag{34}$$

such that f_{R} is the sum of the volume fractions of all families of fibers in $\mathcal{B}_{\mathrm{R}}$, and therefore $(1-f_{\mathrm{R}})$ is the total volume fraction of swellable polymer matrix in $\mathcal{B}_{\mathrm{R}}$. Next, we assume total free energy of the system to be additively decomposed

$$\psi_R = (1 - f_R)\psi_R^{\text{matrix}} + (1 - f_R)\psi_R^{\text{mixing}} + \sum_\gamma f_R^{(\gamma)}\psi_R^{(\gamma),\text{fiber}}, \qquad (35)$$

where ψ_R^{matrix} is the free energy of polymer matrix, ψ_R^{mixing} is the free energy of mixing between polymer matrix and solvent, and $\psi_R^{(\gamma),\text{fiber}}$ is the free energy of each fiber family.

5.1.1. *Mechanical free energy of the polymer matrix*

Following the literature, and using (6), we define the effective stretch, $\bar{\lambda}$, which includes both mechanical and swelling deformation, as

$$\bar{\lambda} \overset{\text{def}}{=} \sqrt{\frac{1}{3}\text{tr }\mathbf{C}} = \frac{1}{\sqrt{3}}(1 + \Omega c_R)^{1/3}\sqrt{\text{tr }\mathbf{C}^m}. \qquad (36)$$

For capturing the mechanical behavior of the polymer matrix, we use a non-Gaussian statistical mechanics based model [3,4], which takes into account limited extensibility of polymer chains (also known as locking),

$$\psi_R^{\text{matrix}} = G_0\lambda_L^2\Big[\Big(\frac{\bar{\lambda}}{\lambda_L}\Big)\beta + \ln\Big(\frac{\beta}{\sinh\beta}\Big) - \Big(\frac{1}{\lambda_L}\Big)\beta_0 - \ln\Big(\frac{\beta_0}{\sinh\beta_0}\Big)\Big] - G_0\left(\frac{\lambda_L}{3}\ln J\beta_0\right) + J^s\Big[\frac{1}{2}K\ln J^m\Big], \qquad (37)$$

with $\beta = \mathcal{L}^{-1}\left(\frac{\bar{\lambda}}{\lambda_L}\right)$ and $\beta_0 = \mathcal{L}^{-1}\left(\frac{1}{\lambda_L}\right)$, where $\mathcal{L}^{-1}$ is the inverse of the Langevin function $\mathcal{L}(\bullet) = \coth(\bullet) - (\bullet)^{-1}$. This form of mechanical free energy includes two material parameters, the initial shear modulus G_0, and the locking stretch λ_L. The locking stretch λ_L has the physical interpretation of the limiting value of the effective stretch $\bar{\lambda}$, when the chains are fully extended.

5.1.2. *Mixing free energy*

For our estimate of mixing free energy we implement the well known Flory–Huggins model [21,31] which takes into account mixing of solvent molecules and the polymer matrix in the form

$$\psi_R^{\text{mixing}} = \mu^0 c_R + R\vartheta c_R\left(\ln\Big(\frac{\Omega c_R}{1 + \Omega c_R}\Big) + \chi\Big(\frac{1}{1 + \Omega c_R}\Big)\right). \qquad (38)$$

Here, μ^0 is a reference chemical potential, R is the gas constant, ϑ is absolute temperature, and χ is a dimensionless polymer-solvent interaction parameter.

5.1.3. *Mechanical free energy for the fibers*

To account for mechanical free energy for the embedded fibers we adopt the form found in Holzapfel [28] which is also used in Nardinocchi et al. [40]. Following the approach discussed in Section 2.1, the contribution due to the fibers is modeled using

$$\psi_R^{(\gamma),\text{fiber}} = \frac{1}{2}E^{(\gamma)}(I_4^{(\gamma)} - 1)^2, \qquad (39)$$

with $E^{(\gamma)}$ the fiber modulus for each fiber family γ. Also, recall that $I_4^{(\gamma)}$ defined in (2) includes the dependence on orientation. Thereby, we incorporate the influence of different fiber families, which may have a different fiber modulus and/or orientation, and volume fraction through $f_R^{(\gamma)}$ as seen in (35).

5.1.4. *Total free energy*

Combining the mechanical free energy of the polymer matrix (37), the mechanical free energy of the embedded fibers (39), along with the mixing free energy (38) into (35), we obtain the total free energy

$$\psi_R = (1 - f_R)\Big\{G_0\lambda_L^2\Big[\Big(\frac{\bar{\lambda}}{\lambda_L}\Big)\beta + \ln\Big(\frac{\beta}{\sinh\beta}\Big) - \Big(\frac{1}{\lambda_L}\Big)\beta_0 - \ln\Big(\frac{\beta_0}{\sinh\beta_0}\Big)\Big] - G_0\left(\frac{\lambda_L}{3}\ln J\beta_0\right) + \mu^0 c_R + R\vartheta c_R\left(\ln\Big(\frac{\Omega c_R}{1 + \Omega c_R}\Big) + \chi\Big(\frac{1}{1 + \Omega c_R}\Big)\right) + J^s\Big[\frac{1}{2}K\ln J^m\Big]\Big\} + \sum_\gamma f_R^{(\gamma)}\frac{1}{2}E^{(\gamma)}(I_4^{(\gamma)} - 1)^2. \qquad (40)$$

5.2. *Cauchy stress*

Following (32), and using (40), we obtain the Cauchy stress

$$\begin{aligned}\mathbf{T} &= J^{-1}\left(2\mathbf{F}^m\frac{\partial\bar{\psi}_R(\mathbf{C}^m, c_R)}{\partial\mathbf{C}^m}\mathbf{F}^{m\top}\right)\\ &= J^{-1}\underbrace{(1 - f_R)\Big(G_0\big(\zeta\phi^{-2/3}\mathbf{B}^m - \zeta_0\mathbf{1}\big) + J^sK(\ln J^m)\mathbf{1}\Big)}_{\text{contribution due to the polymer matrix}}\\ &\quad + J^{-1}\underbrace{\sum_\gamma 2f_R^{(\gamma)}E^{(\gamma)}(\lambda^s)^2(I_4^{(\gamma)} - 1)\mathbf{F}^m(\mathbf{a}_R^{(\gamma)}\otimes\mathbf{a}_R^{(\gamma)})\mathbf{F}^{m\top}}_{\text{contribution due to the fibers}},\end{aligned} \qquad (41)$$

with

$$\zeta \overset{\text{def}}{=} \Big(\frac{\lambda_L}{3\bar{\lambda}}\Big)\mathcal{L}^{-1}\Big(\frac{\bar{\lambda}}{\lambda_L}\Big) \text{ and } \zeta_0 \overset{\text{def}}{=} \Big(\frac{\lambda_L}{3}\Big)\mathcal{L}^{-1}\Big(\frac{1}{\lambda_L}\Big). \qquad (42)$$

From (41) it is clear that the volume fraction of embedded fibers $f_R^{(\gamma)}$ determines the contribution of each constituent of the system. The influence of the polymer matrix to the Cauchy stress decreases with f_R, however, the importance of the embedded fibers increases with f_R. Further, the stiffness of the polymer matrix decreases with solvent concentration through terms related to ϕ. Further, since there is no mixing between the solvent and the embedded fibers, the embedded fibers tend to constrain the swelling process. Lastly, it is worth noting that due to (3) and (2), the embedded fibers have an affect on both swelling and mechanical deformation.

5.3. *Chemical potential*

Next, using (40) and (33), we obtain the chemical potential in the form

$$\begin{aligned}\mu &= \frac{\partial\psi_R}{\partial c_R} - \Omega\frac{1}{3}J^m\text{tr }\mathbf{T}\\ &= \underbrace{(1 - f_R)\Big[\mu^0 + R\vartheta\Big(\ln(1 - \phi) + \phi + \chi^p\phi^2\Big)\Big]}_{\text{mixing contribution}}\\ &\quad \underbrace{-(1 - f_R)\Big[\Omega K(\ln J^e) - \frac{1}{2}K\Omega(\ln J^e)^2\Big]}_{\text{matrix “mechanical” contribution}}\\ &\quad \underbrace{+f_R\Big[\frac{2}{3}E\Omega(1 + \Omega c_R)I_4(I_4 - 1)\Big]}_{\text{fiber “mechanical” contribution}}.\end{aligned} \qquad (43)$$

Here, it can be observed that the chemical potential is not only affected by the mixing of polymer matrix and solvent, but also by the mechanical deformation of the fiber-reinforced polymeric gel. The mechanical pressure and its energy, along with the deformation of embedded fibers, contributes to the chemical potential of the system, thus fully coupling the mechanical and chemical aspects of gel behavior.

Table 1
Material parameters used in the numerical simulations.

	Parameter	Value
Polymer Matrix	G_0	1 MPa
	K	100 MPa
	λ_L	10.0
Solvent	Ω	1×10^{-4} m^3/mol
	μ^0	0.0 J/mol
Interaction	χ	0.2
Fibers	$E^{(\gamma)}$	1 GPa

5.4. Mobility tensor

The solvent mobility tensor, which takes into account any possible anisotropy in diffusion, is assumed to be temperature and concentration dependent, and is given in the form

$$\mathbf{M} = \mathbf{D}\frac{c}{R\vartheta} = \mathbf{D}\frac{c_{\mathrm{R}}}{JR\vartheta}, \tag{44}$$

where $\mathbf{D}$ and $c = J^{-1}c_{\mathrm{R}}$ represent the tensorial diffusivity and the solvent concentration per unit spatial volume, respectively. The tensorial form of the diffusivity allows for the inclusion of anisotropic diffusion response. In practice it is generally more convenient to use ϕ in place of c since ϕ is bounded, $0 < \phi \leq 1$. Accordingly, using (17) we rewrite (44) in the form

$$\mathbf{M} = \mathbf{D}\left(\frac{1-\phi}{R\vartheta J\Omega\phi}\right). \tag{45}$$

Also, as previously mentioned in Section 4, the mobility tensor $\mathbf{M}$ must be positive definite based on the free energy imbalance (28). As a further consequence, we take the diffusivity tensor $\mathbf{D}$ to be positive definite.

6. Model behavior through numerical simulations

In this section, we present the capabilities of our anisotropic deformation-diffusion constitutive model for polymeric gels with embedded fibers by solving various boundary value problems. We note that details for the governing equations and finite element implementation are provided in an Appendix, Section 9. In this section we consider both two dimensional plane strain swelling, and three-dimensional free swelling. Specifically we consider an initial dry body with a square/cube shape having an edge length of 2 mm under a constant isothermal temperature of 298 K. In both cases the body is traction free, undergoing essentially free swelling, however in plane strain the third dimension is constrained. The specific simulations that follow first probe the constitutive model when (i) the diffusion is anisotropic without fibers, (ii) a single family of fibers are present and the diffusion is isotropic, and lastly (iii) when a single family of fibers and anisotropic diffusion are present. Specific values for the material parameters that remain unchanged across all the numerical simulations that follow are provided in Table 1.

6.1. Boundary value problem setup

Here, we define the boundary value problem which will be solved to present the model behavior. Fig. 1 shows both plane strain and three-dimensional situations. As shown in Fig. 1, the body is symmetric, and therefore we only model 1/4 in plane strain, or 1/8 in three dimensions. We note that in all simulations that follow, fiber directions are chosen to maintain this symmetry throughout.

For these swelling simulations, the initial dry body is immersed into a solvent bath at a constant temperature of 298 K. With reference to Fig. 1, the corresponding mechanical boundary conditions are:

- symmetry on all relevant planes — faces AB and AD in plane strain, and faces ABCD, ABEF, and ADGE in 3D;
- traction free on all other faces — faces BC and CD in plane strain, and faces BCHF, CDHG, and EFGH in 3D;

and the corresponding chemical boundary conditions are:

- no flux on all symmetry planes — faces AB and AD in plane strain, and faces ABCD, ABEF, and ADGE in 3D;
- a prescribed chemical potential $\tilde{\mu}(t) = \mu^0 + \mu_0 \exp(-t/t_d)$ on faces in contact with solvent — faces BC and CD in plane strain, and faces BCHF, CDHG, and EFGH in 3D. Here $t_d = 200$ s is a decay time used to apply the chemical potential boundary condition smoothly, and μ_0 is the initial chemical potential at time $t = 0$, obtained using (43).

6.2. Anisotropic diffusion in the absence of fibers

To emphasize the affect that anisotropic diffusion has on the deformation, we simulate a polymeric gel without embedded fibers. Thus, we take $f_{\mathrm{R}} = 0$ and prescribe the diffusivity tensor in the form (referring to the coordinate basis as shown in Fig. 1)

$$\begin{aligned} \mathbf{D} &= \begin{bmatrix} 10 & 0 \\ 0 & 1 \end{bmatrix} \times 10^{-9}\mathrm{m}^2/\mathrm{s} \quad \text{and} \\ \mathbf{D} &= \begin{bmatrix} 10 & 0 & 0 \\ 0 & 1 & 0 \\ 0 & 0 & 10 \end{bmatrix} \times 10^{-9}\mathrm{m}^2/\mathrm{s} \end{aligned} \tag{46}$$

for plane strain and 3D, respectively. For comparison, we show the results using an isotropic diffusivity, $\mathbf{D} = \left(1 \times 10^{-8}\mathbf{1}\right)$ m^2/s, with the same boundary conditions mentioned above.

Fig. 2 shows contours of ϕ at a few snapshots in time for the isotropic and anisotropic simulations. The simulation results in Fig. 2 show the clear difference between the behavior of the isotropic and anisotropic diffusivity in the deformation-diffusion behavior of the polymeric gel. The decreased diffusivity in the $\mathbf{e}_2$ direction leads to noticeably slower diffusion and corresponding swelling along that direction, leading to an observable anisotropy in the overall response of a gel. However, as expected, after long times, where diffusion is no longer driving solvent at equilibrium, there is no difference between the isotropic and anisotropic results.

6.3. Isotropic diffusion with embedded fibers

Next, we consider isotropic diffusion, but with the influence of embedded fibers. To observe the influence of the fiber volume fraction, we consider only a single fiber family with a fiber direction $\mathbf{a}_{\mathrm{R}} = \mathbf{e}_1$ (referring to the coordinate basis as shown in Fig. 1), for both plane strain and three-dimensional simulations. For comparison, we show the results using an isotropic gel without any fibers, and, in all cases we take $\mathbf{D} = \left(1 \times 10^{-8}\mathbf{1}\right)$ m^2/s. Then, we vary the fiber volume fraction, choosing

$$f_{\mathrm{R}} = \{1 \times 10^{-3},\ 5 \times 10^{-3},\ 1 \times 10^{-2},\ 5 \times 10^{-2},\ 1 \times 10^{-1}\}.$$

in the simulations that follow.

Fig. 3 shows contours of ϕ at a few snapshots in time for the isotropic and anisotropic simulations with $f_{\mathrm{R}} = 1 \times 10^{-1}$. The results of numerical simulation in Fig. 3 clearly show that, due to the

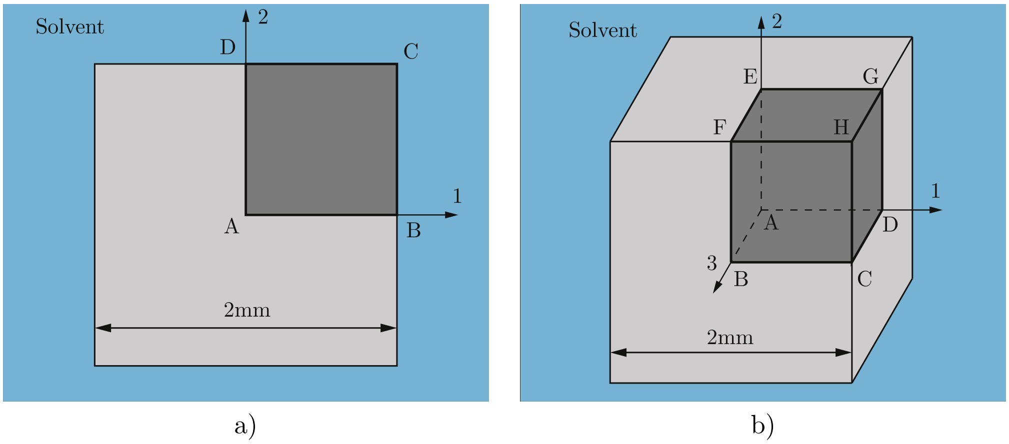

Fig. 1. Schematic of an initially dry 2 mm (a) square and (b) cube, immersed in solvent. For the numerical simulation, due to symmetry, we mesh only mesh the portion of the body indicated in dark grey.

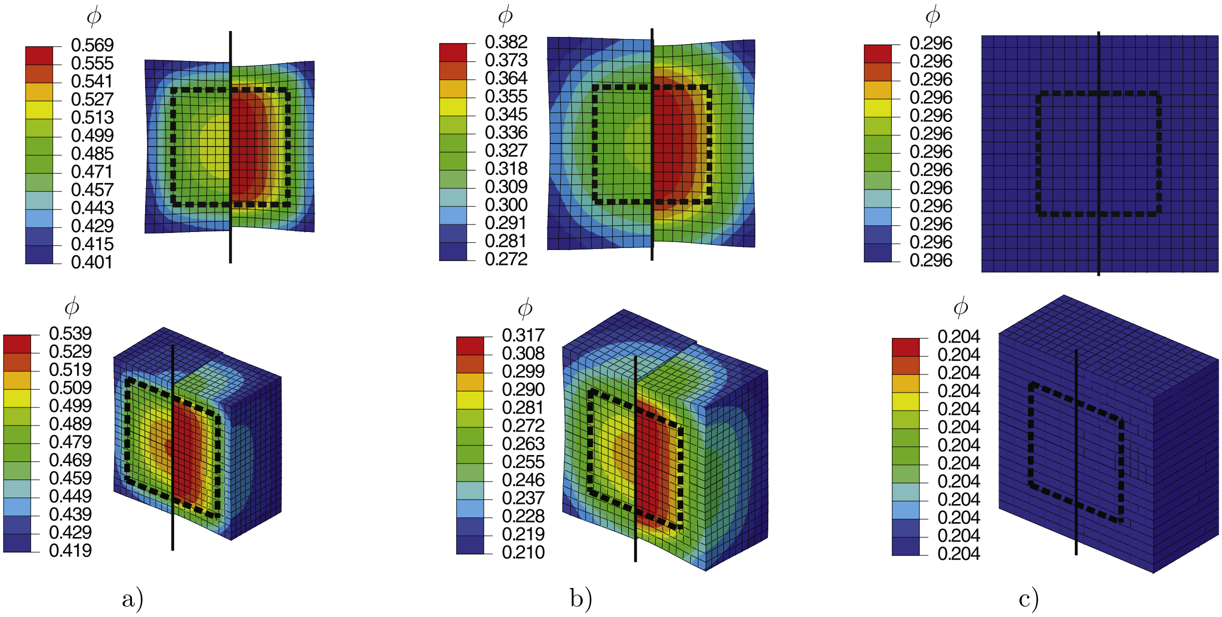

Fig. 2. Simulation results showing ϕ at (a) 900 s, (b) 1800 s, and (c) 6 h, in plane strain (top) and 3D (bottom). In all cases, to help with comparison, the left portion is the isotropic simulation, while the right portion is anisotropic diffusion in the absence of fibers. Further, the thick dotted line indicates the initial dry body.

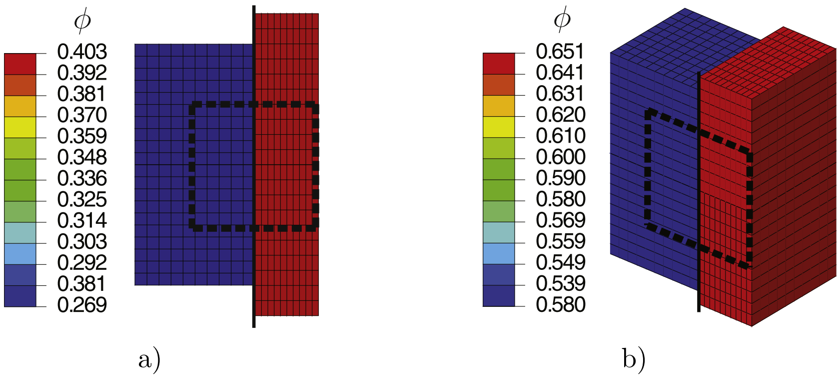

Fig. 3. Simulation results showing ϕ at 6 h for (a) plane strain, and (b) 3D. In both cases, to help with comparison, the left portion is the isotropic simulation, while the right portion is anisotropic, with fiber direction $\mathbf{a}_R = \mathbf{e}_1$ and volume fraction $f_R = 10^{-1}$. Further, the thick dotted line indicates the initial dry body.

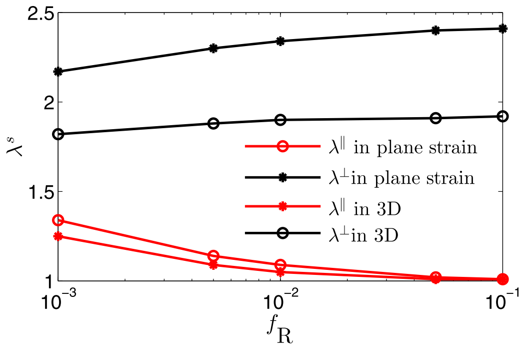

Fig. 4. Simulation results showing the stretch along the fiber direction, $\lambda^{\parallel}$, and that perpendicular to it $\lambda^{\perp}$ near equilibrium at 6 h for various fiber volume fractions.

constrained swelling caused by the embedded fibers, the swelling stretch along the fiber direction is significantly lower than that in the other directions. That difference is further quantified in Fig. 4, where the stretch along the fiber direction $\lambda^{\parallel}$ decreases with the increase in fiber volume fraction. This is accompanied by an increase in the swelling stretch along the other directions, indicated by $\lambda^{\perp}$.

6.4. Anisotropic diffusion with embedded fibers

In this section, we perform simulations that include both embedded fibers and anisotropic diffusion. To keep results easy to interpret, we take a single fiber direction with $\mathbf{a}_R = \mathbf{e}_2$ at a volume fraction of $f_R = 1 \times 10^{-1}$, and assume the diffusivity to be (referring to the coordinate basis as shown in Fig. 1)

$$\mathbf{D} = \begin{bmatrix} 10 & 0 \\ 0 & 1 \end{bmatrix} \times 10^{-9}\mathrm{m}^2/\mathrm{s} \quad \text{and}$$
$$\mathbf{D} = \begin{bmatrix} 10 & 0 & 0 \\ 0 & 1 & 0 \\ 0 & 0 & 10 \end{bmatrix} \times 10^{-9}\mathrm{m}^2/\mathrm{s} \qquad (47)$$

for plane strain and 3D, respectively. As previously mentioned, we assume the embedded fibers unable to swell, causing the solvent transport to be impeded along the fiber direction. Accordingly, we take the solvent diffusivity to be significantly slower in the direction of embedded fibers. Similar to the simulation results presented thus far, we again compare against an isotropic polymeric gel in the absence of embedded fibers, using an isotropic diffusivity $\mathbf{D} = \left(1 \times 10^{-8}\mathbf{1}\right)\ \mathrm{m}^2/\mathrm{s}$.

Fig. 5 shows contours of ϕ at a few snapshots in time for the isotropic and anisotropic simulations. The simulation results, under both plane stain and three-dimensional conditions, display pronounced anisotropy which is easily observed in Fig. 5. Due to the combined influence of solvent diffusion anisotropy and the mechanical response of embedded fibers, the deformation is significantly constrained along the $\mathbf{e}_2$ direction, while the gel is allowed to freely swell in the other directions. Opposed to the example in Section 6.2, even when the equilibrium is reached, after 6 h of free swelling there is a significant difference between isotropic and anisotropic simulations, due entirely to the presence of embedded fibers.

7. Diffusion activated soft gripper: Qualitative comparison between experiment and simulation

As a final exercise of the model, we qualitatively compare our simulation results with experiments of a soft robotic gripper. Since the materials used in the experiment have not yet been characterized, our comparison is only qualitative, and we continue using the material parameters provided in Table 1.

The construction of the diffusion activated soft gripper consists of two arms of fiber-reinforced polymer gel connected to a rigid glass plate. The two arms are composed of polyethylene glycol diacrylate (PEGDA 700) and off-the-shelf medical gauze to used for the embedded fibers. To manufacture the soft gripper, a photocurable precursor solution is prepared by mixing PEGDA 700, as a monomer, and 43 mM of phenylbis(2,4,6-trimethylbenzoyl) phosphine oxide as a photo-initiator. A piece of medical gauze, with approximately a 0.5 mm thickness is placed on a transparent glass mold. The precursor solution is then poured into the mold, up to 1.5 mm from the bottom, and polymerized using ultraviolet (UV) illumination, with an exposure energy of 250 mJ/cm^2. As a result, a 1.5 mm thick composite polymer film is formed, with a 0.5 mm thick fiber network embedded on the bottom as can be seen in Fig. 6a. The composite polymer film is cut into the 57 mm long and 3.5 mm wide strips as in Fig. 6b. Two fiber-embedded composite polymer strips, serving as gripper arms, are bonded to a glass plate using super glue. The arms are oriented with the fiber-reinforced side facing downward, with the angle between the arms 70° as shown in Fig. 7.

In the experiment, shown in Fig. 8, the full gripper is submerged into solvent, in this case water, and the subsequent diffusion and anisotropic swelling due to the embedded fibers causes the gripper arms to bend and close onto a block. This mode of deformation is utilized for grabbing and subsequently moving the block.

For the finite element simulation, due to the symmetry of the gripper, we mesh only a quarter of the geometry, i.e. a half of 1 arm. The structured finite element mesh of the gripper consists of 6,958 three-dimensional 8-node brick user-elements. Also, since the gripper arms are constructed with embedded fibers only close to the bottom of the arms, we model two distinct layers through the thickness — the bottom with fibers embedded; and an isotropic top layer without fibers. Specifically, the top layer is taken to be 1 mm thick as shown in Fig. 9, and since there are no embedded fibers, $f_R = 0$, with an isotropic solvent diffusivity $\mathbf{D} = \left(1.5 \times 10^{-8}\mathbf{1}\right)\ \mathrm{m}^2/\mathrm{s}$. The bottom layer is taken to be 0.5 mm thick, and contains two families of embedded fibers oriented perpendicular to each other with directions, $\mathbf{a}_R^{(1)} = \mathbf{e}_{1'}$ and $\mathbf{a}_R^{(2)} = \mathbf{e}_{3'}$, written in the local coordinate system as shown in Fig. 9. Additionally, we choose the fiber volume fraction to be the same for both orientations, and relatively small based on Fig. 6c, specifically $f_R^{(1)} = f_R^{(2)} = 10^{-2}$. Since the bottom layer contains fibers, we assume the diffusivity to be slightly anisotropic, and we take

$$\mathbf{D} = \begin{bmatrix} 1.0 & 0.0 & 0.0 \\ 0.0 & 1.5 & 0.0 \\ 0.0 & 0.0 & 1.0 \end{bmatrix} \times 10^{-8}\mathrm{m}^2/\mathrm{s} \qquad (48)$$

in the local $1' - 2' - 3'$ coordinate system as shown in Fig. 9.[2]

To realistically simulate the experiment, we include a non-swellable block with edge length 2 mm that will be picked up by the soft gripper. We assume the block is much stiffer than the soft gripper and model the block as linear elastic with modulus 5 GPa. The interaction between the soft gripper and the block is modeled with a rough contact interaction, meaning no slip. For visualization purposes, a rigid body is included in the simulation to model the glass plate from the experiment, and the soft gripper is bonded to this glass plate in the simulation such that it may swell along $\mathbf{e}_2$, but is fully constrained in $\mathbf{e}_1$.

Considering Fig. 9, the mechanical boundary conditions prescribed for this simulation are:

---

[2] We note that both the fiber directions, and diffusivity, given here in local coordinate system $1' - 2' - 3'$, are later rotated to the global coordinate system $1 - 2 - 3$ inside the finite element simulation.

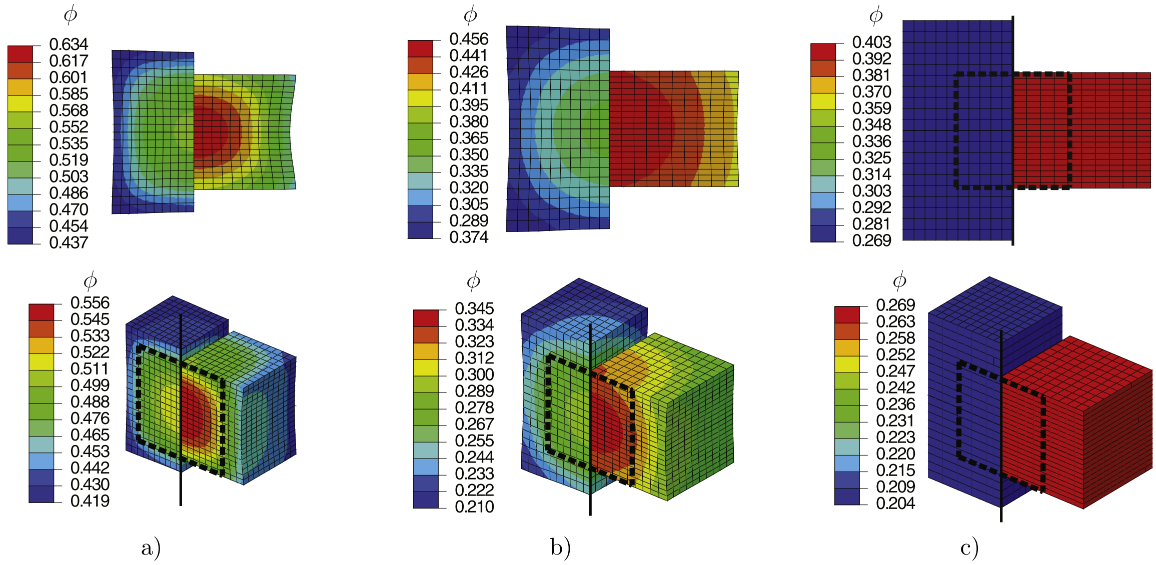

Fig. 5. Simulation results showing ϕ at (a) 900 s, (b) 1800 s, and (c) 6 h, in plane strain (top) and 3D (bottom). In all cases, to help with comparison, the left portion is the isotropic simulation, while the right portion is anisotropic diffusion with fiber direction $\mathbf{a}_R = \mathbf{e}_2$ and $f_R = 10^{-1}$. Further, the thick dotted line indicates the initial dry body.

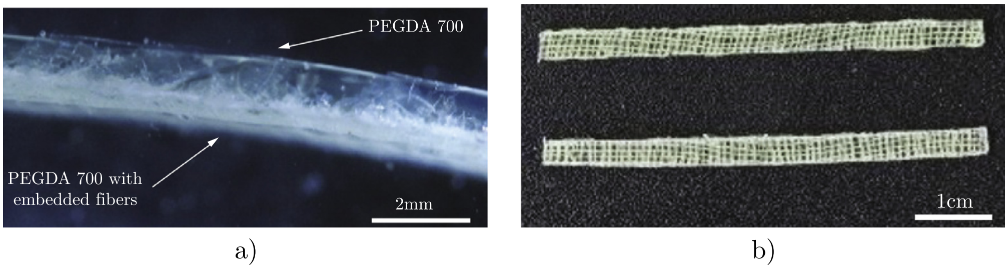

Fig. 6. Manufacture of the composite gripper arm. (a) Shows medical gauze embedded in the lower portion of the body, and (b) shows the two strips used to construct the soft gripper, prior to bonding in the initial dry state.

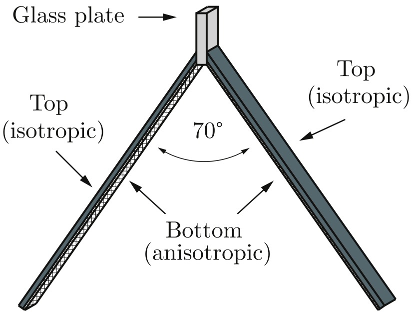

Fig. 7. Schematic of the soft gripper assembly. The gripper arms are bonded to a glass plate with the fiber-reinforced side facing downward.

- Symmetry boundary conditions are prescribed on the 1–2 and 2–3 planes.
- The displacement on face A-A is mechanically constrained along the 1-direction. In addition, the top node on face A-A is pinned.
- The glass plate is fully constrained, while the block is traction free on all faces.

Next, to account for the immersion in solvent, the chemical potential is prescribed on the external faces of the gripper, except for the face bonded to the glass plate. As before, the chemical potential is prescribed in the form $\breve{\mu}(t) = \mu^0 + \mu_0 \exp(-t/t_d)$ to smoothly apply the chemical potential boundary condition.

Fig. 10 shows contours of ϕ in the simulation of the soft gripper working at various snapshots in time. The initially dry soft gripper, shown in Fig. 10a, is immersed in solvent and through diffusion begins to swell and deform. The bottom layer of the gripper, which contains the embedded fibers and has an anisotropic diffusivity, swells less than the top layer. This constrained swelling of the bottom layer, forces the arms to bend, and eventually close in and grab the block. Finally, the block is picked up and may be moved elsewhere.

Comparing our numerical simulation with the experimentally observed operation of a soft gripper, we have qualitative agreement between the two. In both cases, the presence of the embedded fibers on the bottom side of the soft gripper leads to constrained swelling, which in turn causes the gripper to close and grab the block. Therefore, the constitutive model and it's numerical implementation may provide a qualitative tool for the design of soft robotic devices.

8. Concluding remarks

We have developed a continuum-level model to capture the major features of fiber-reinforced polymeric gel behavior. The anisotropic aspects of the model are (i) the influence of non-linear elastic embedded fibers that do not swell inside the polymer matrix, and (ii) anisotropic diffusion of solvent within the polymer matrix. The mechanical response of the polymer matrix is described using a non-Gaussian statistical-mechanical model, along with Flory–Huggins model for mixing free energy.

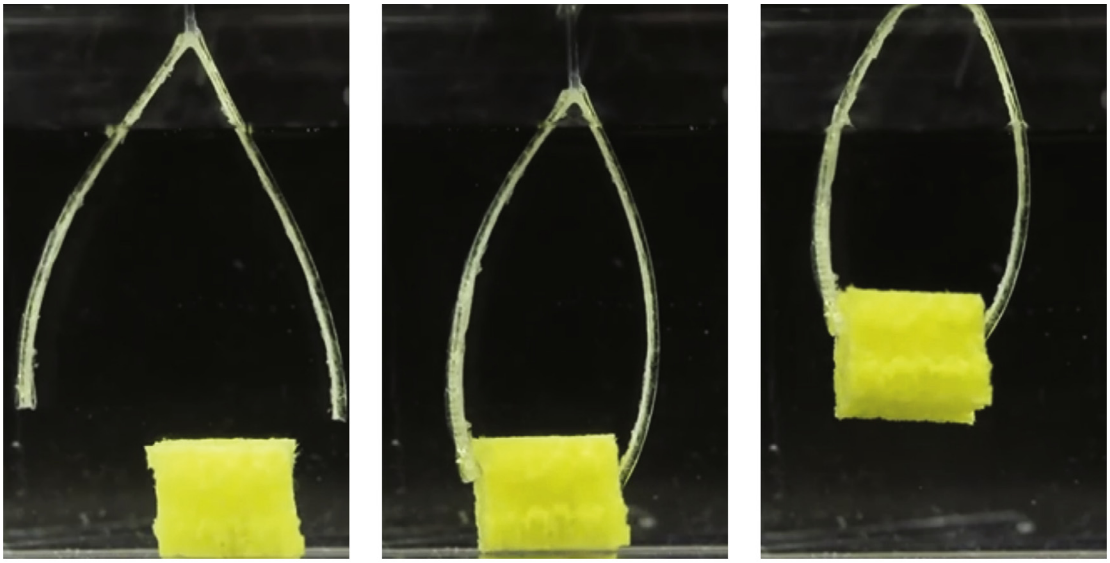

a) b) c)

Fig. 8. Experimental results showing the operation of diffusion activated soft gripper. (a) Initially after immersion into water, (b) the embedded fibers cause anisotropic swelling to make the gripper arms close in and grab the block, and (c) lifting the block.

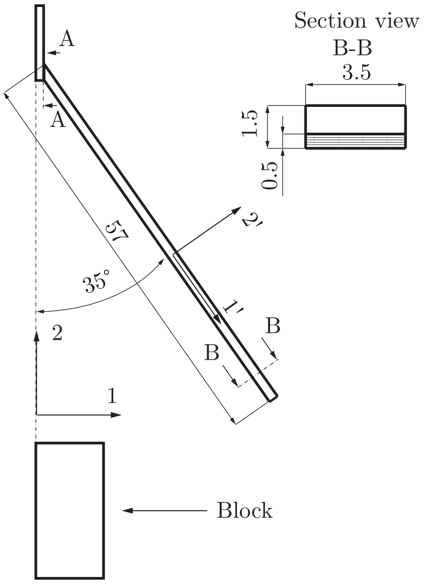

Fig. 9. Schematic of the soft gripper assembly that is used in the numerical simulation, indicating the local coordinate system used for material properties, as well as the layers with and without fibers.

The constitutive model has been numerically implemented in a commercially available software package Abaqus/Standard [1] by writing a user element subroutine (UEL). That numerical implementation was utilized for solving boundary-value problems which showcase the capabilities of the model to simulate the behavior of fiber-reinforced polymeric gels.

Lastly, we have constructed a diffusion activated soft gripper and experimentally observed its operation. Using the numerical implementation of the constitutive model, we were able to simulate the operation of our soft gripper. Qualitative comparison of experiment and simulation shows good agreement between the two, thus displaying the capabilities of our model to account for the major features of fiber-reinforced polymeric gel behavior.

Nonetheless, in the current literature on gel mechanics, there is a lack of experimental data required for the calibration of constitutive models. Towards the future, improvements in experimental methods and experimental data focused on mechanics would allow the refinement and validation of constitutive models.

Acknowledgments

SAC acknowledges support from the National Science Foundation (CMMI-1463121 and CMMI-1751520).

Appendix. Governing equations and finite-element implementation

In the absence of body forces and inertial effects, the governing partial differential equations, expressed in the deformed body $\mathcal{B}_t$, consist of the balance of forces and the balance of solvent content. The balance of forces yields

$$\operatorname{div}\mathbf{T} = \mathbf{0} \quad \text{in} \quad \mathcal{B}_t, \tag{49}$$

with the Cauchy stress $\mathbf{T}$ given by (41). And the balance of solvent content yields

$$\frac{\dot{\phi}}{J\Omega\phi^2} + \operatorname{div}\mathbf{j} = 0 \quad \text{in} \quad \mathcal{B}_t, \tag{50}$$

with the fluid flux $\mathbf{j}$ given by (30) and the mobility by (45). With the displacement denoted by $\mathbf{u}(\mathbf{x}, t)$, the mechanical boundary conditions on $\partial\mathcal{B}_t$ are given by

$$\mathbf{u} = \breve{\mathbf{u}} \quad \text{on} \quad \mathcal{S}_{\mathbf{u}}, \quad \text{and} \quad \mathbf{T}\mathbf{n} = \breve{\mathbf{t}} \quad \text{on} \quad \mathcal{S}_{\mathbf{t}}, \tag{51}$$

where $\breve{\mathbf{u}}$ and $\breve{\mathbf{t}}$ are the prescribed displacements and spatial surface tractions, respectively, and $\mathcal{S}_{\mathbf{u}}$ and $\mathcal{S}_{\mathbf{t}}$ are complementary subsurfaces of $\partial\mathcal{B}_t$. The chemical boundary conditions on $\partial\mathcal{B}_t$ are given by

$$\mu = \breve{\mu} \quad \text{on} \quad \mathcal{S}_{\mu}, \quad \text{and} \quad -\mathbf{j}\cdot\mathbf{n} = \breve{j} \quad \text{on} \quad \mathcal{S}_{\mathbf{j}}, \tag{52}$$

where $\breve{\mu}$ and $\breve{j}$ are the prescribed chemical potential and spatial surface flux, respectively, and $\mathcal{S}_{\mu}$ and $\mathcal{S}_{\mathbf{j}}$ are another set of complementary subsurfaces of $\partial\mathcal{B}_t$. The initial conditions are taken as

$$\mathbf{u}(\mathbf{x}_{\mathrm{R}}, 0) = \mathbf{u}_0 \quad \text{and} \quad \mu(\mathbf{x}_{\mathrm{R}}, 0) = \mu_0 \quad \text{in} \quad \mathcal{B}_{\mathrm{R}}. \tag{53}$$

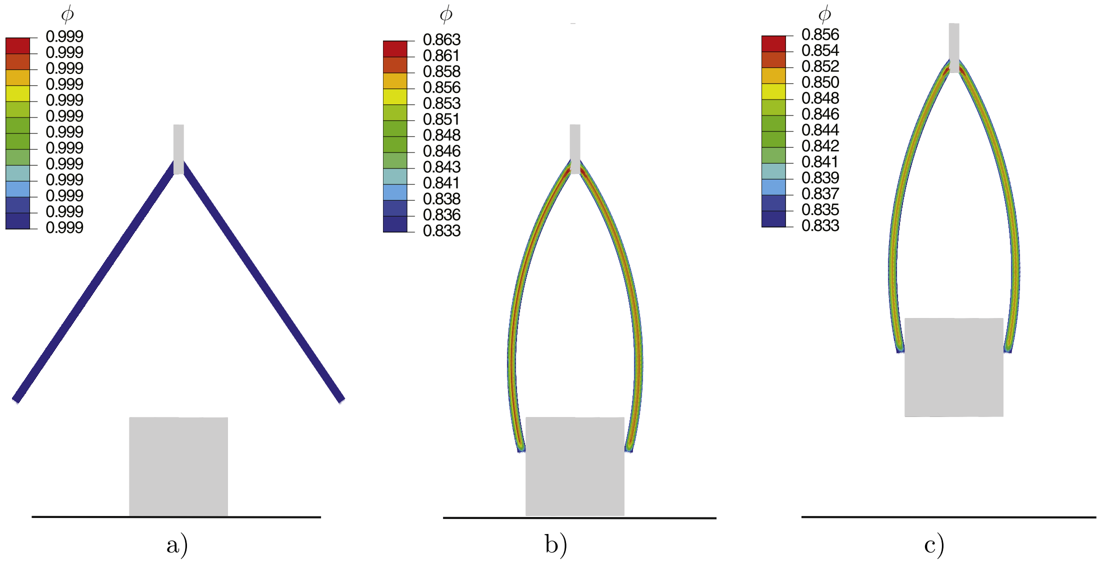

Fig. 10. Simulation results showing ϕ during operation of diffusion activated soft gripper. (a) The initial state immediately after immersion in water, (b) the embedded fibers cause anisotropic swelling to make the gripper arms close in and grab the block, and (c) lifting the block.

The coupled set of equations (49) and (50), along with the boundary conditions (51) and (52), and initial conditions (53), represents the strong form of the initial boundary value problem for the displacement field and the chemical potential field.

With $\mathbf{w}_1$ and w_2 denoting two weighting fields, the weak form of the boundary-value problem (49) through (52) is

$$\begin{cases} \int_{\mathcal{B}_t} \left(\mathbf{T} : \dfrac{\partial \mathbf{w}_1}{\partial \mathbf{x}} \right) dv = \int_{\mathcal{S}_\mathbf{t}} \left(\mathbf{w}_1 \cdot \breve{\mathbf{t}} \right) da, \\ \int_{\mathcal{B}_t} \left(\frac{w_2 \dot{\phi}}{J\Omega\phi^2} \right) dv = \int_{\mathcal{B}_t} \left(\mathbf{j} \cdot \dfrac{\partial w_2}{\partial \mathbf{x}} \right) dv + \int_{\mathcal{S}_\omega} \left(w_2 \breve{j} \right) da. \end{cases}$$

Following our previous work [13,14], the deformed body is approximated using finite elements, $\mathcal{B}_t = \cup \mathcal{B}_t^{\mathrm{e}}$, and the nodal degrees of freedom are the displacement and the chemical potential, which are interpolated inside each element by

$$\mathbf{u} = \sum \mathbf{u}^A N^A \quad \text{and} \quad \mu = \sum \mu^A N^A, \tag{54}$$

with the index $A = 1, 2, \ldots$ denoting the nodes of the element, $\mathbf{u}^A$ and μ^A the nodal displacements and chemical potentials, and N^A the shape functions. Employing a standard Galerkin approach, in which the weighting fields $\mathbf{w}_1$ and w_2 are interpolated by the same shape functions, leads to the following element-level residuals

$$\left. \begin{aligned} (\mathbf{R}_\mathbf{u})^A &= -\int_{\mathcal{B}_t^e} \left(\mathbf{T} \frac{\partial N^A}{\partial \mathbf{x}} \right) dv + \int_{\mathcal{S}_\mathbf{t}^e} \left(N^A \breve{\mathbf{t}} \right) da, \\ (R_\mu)^A &= \int_{\mathcal{B}_t^e} \left(\frac{N^A \dot{\phi}}{J\Omega\phi^2} \right) dv + \int_{\mathcal{B}_t^e} \left(\mathbf{j} \cdot \frac{\partial N^A}{\partial \mathbf{x}} \right) dv \\ &\quad + \int_{\mathcal{S}_\mathbf{j}^e} \left(N^A \breve{j} \right) da. \end{aligned} \right\} \tag{55}$$

These element-level residuals are assembled into a global residual, which represents a non-linear system of equations for the nodal degrees of freedom.

Correspondingly, four element level tangents are required for the iterative Newton–Raphson solution procedure. The first tangent accounts for changes in the displacement residual with respect to the displacement, and is given by

$$K_{u_i u_k}^{AB} = -\frac{\partial R_{u_i}^A}{\partial u_k^B} = \int_{\mathcal{B}_t^e} \frac{\partial N^A}{\partial x_j} \mathbb{A}_{ijkl} \frac{\partial N^B}{\partial x_l} dv - \int_{\mathcal{S}_\mathbf{t}^e} N^A N^B \frac{\partial \breve{t}}{\partial u_k} da, \tag{56}$$

where the spatial tangent modulus $\mathbb{A}$ is related to the referential tangent modulus $\mathbb{A}_\mathrm{R}$ through

$$\mathbb{A}_{ijkl} = J^{-1} F_{jm} F_{ln} (\mathbb{A}_\mathrm{R})_{imkn}, \tag{57}$$

and the referential tangent modulus is given by $\mathbb{A}_\mathrm{R} \overset{\mathrm{def}}{=} \dfrac{\partial \mathbf{T}_\mathrm{R}}{\partial \mathbf{F}}$. And further,

$$K_{u_i \mu}^{AB} = -\frac{\partial R_{u_i}^A}{\partial \mu^B} = \int_{\mathcal{B}^e} \frac{\partial N^A}{\partial x_j} \left(\frac{\partial T_{ij}}{\partial \phi} \frac{\partial \phi}{\partial \mu} \right) N^B dv, \tag{58}$$

$$K_{\mu u_k}^{AB} = -\frac{\partial R_\mu^A}{\partial u_k^B} = -\int_{\mathcal{B}^e} \frac{\partial N^A}{\partial x_i} \left(M_{il} \frac{\partial \mu}{\partial x_k} \right) \frac{\partial N^B}{\partial x_l} dv, \tag{59}$$

and

$$\begin{aligned} K_{\mu\mu}^{AB} = -\frac{\partial R_\mu^A}{\partial \mu^B} = -\int_{\mathcal{B}^e} \frac{N^A N^B}{J\Omega\phi^2} \left(2 \frac{\dot{\phi}}{\phi} \frac{\partial \phi}{\partial \mu} - \frac{\partial \dot{\phi}}{\partial \mu} \right) dv \\ - \int_{\mathcal{B}^e} \left(\frac{\partial j_i}{\partial \mu} \frac{\partial N^A}{\partial x_i} \right) dv - \int_{\mathcal{S}_\mathbf{j}^e} \left(N^A N^B \frac{\partial \breve{j}}{\partial \mu} \right) da. \end{aligned} \tag{60}$$

Our finite-element procedures have been implemented in commercially available software package Abaqus/Standard [1] using a user-element subroutine (UEL). We have developed a four-noded isoparametric quadrilateral plane-strain user-element, and an eight-noded continuum brick user-element. In order to avoid issues related to volumetric-locking, we utilize the F-bar method of de Souza Neto et al. [17] for fully-integrated elements. For complete details regarding the implementation of Abaqus user-element subroutines for multi-physics problems, readers are referred to Chester et al. [14].

The UEL is verified by comparing analytically tractable solutions against our numerical simulations. Due to the complexity of the fully coupled-scheme in this work, the verifications are done separately on mechanical and diffusion part, respectively. Here, we put our emphasis on the mechanical verification for the inclusion of fibers since the details verifying the diffusion aspects of the UEL have been previously reported in [14].

For the mechanical verification, a simple shear motion is prescribed on a cubic gel embedded with one fiber family with a referential direction of $\mathbf{a}_\mathrm{R}$, the schematic is shown in Fig. 11a.

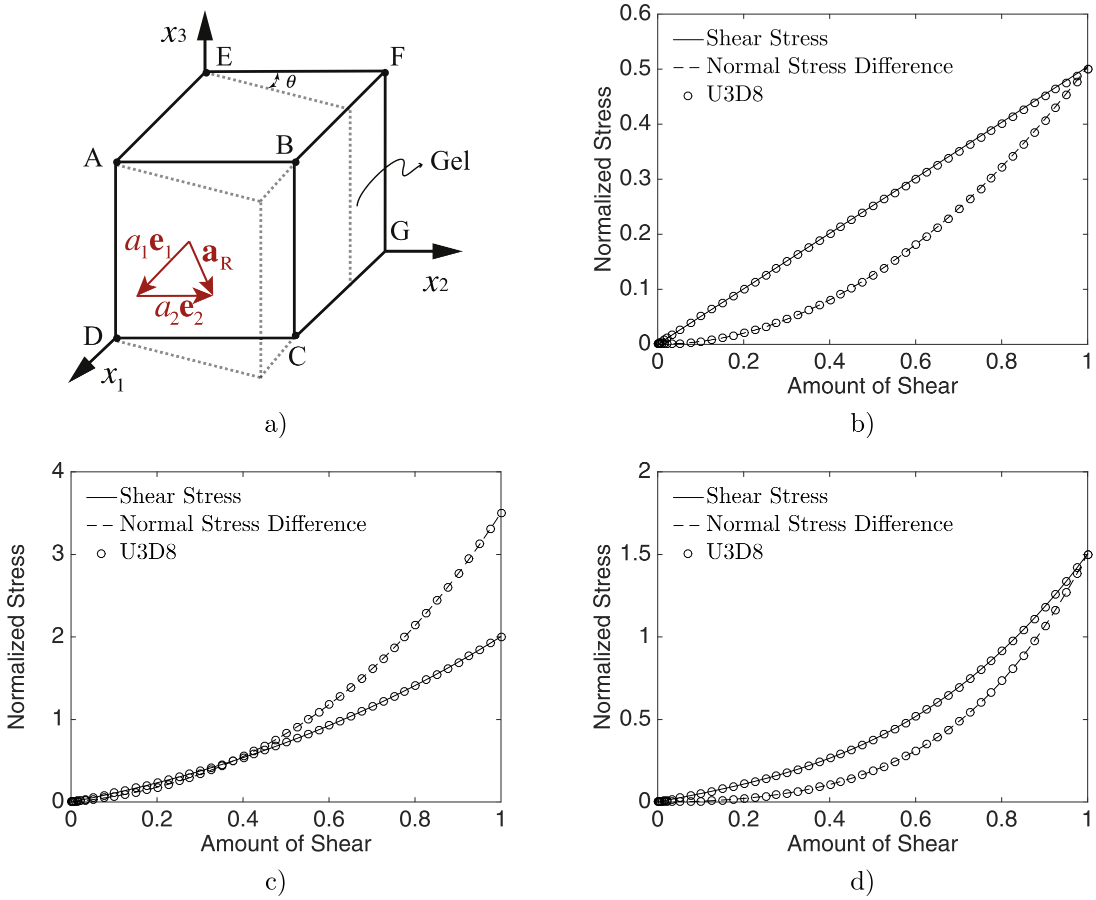

Fig. 11. Comparison between analytical and numerical solutions for simple shear deformation. (a) Schematic of a cubic gel with a single fiber family embedded with referential orientation $\mathbf{a}_\mathrm{R}$ undergoing simple shear deformation. The normalized stress T_{12}/G_0 and normal stress difference $(T_{11}-T_{33})/G_0$ is plotted against the amount of shear $\gamma=\tan\theta$ for different fiber orientations (b) $\mathbf{a}_\mathrm{R}=[1,0,0]^\top$, (c) $\mathbf{a}_\mathrm{R}=[1/\sqrt{2},1/\sqrt{2},0]^\top$, and (d) $\mathbf{a}_\mathrm{R}=[0,1,0]^\top$.

According to Gurtin et al. [25], the corresponding deformation is given by

$$\big[\mathbf{F}\big]=\begin{bmatrix}1 & \gamma & 0\\ 0 & 1 & 0\\ 0 & 0 & 1\end{bmatrix}, \tag{61}$$

where $\gamma=\tan\theta$ denotes the amount of shear. The referential fiber's orientation may be written in the form

$$\mathbf{a}_\mathrm{R}=[a_1,a_2,0]^\top, \tag{62}$$

with a_1 and a_2 denote components in the x_1 and x_2 directions, respectively. Also, to make $\mathbf{a}_\mathrm{R}$ a unit vector, the constraint of $\sqrt{a_1^2+a_2^2}=1$ has to be fulfilled. After taking the tensor product operation of $\mathbf{a}_\mathrm{R}$, the structure tensor $\mathbf{A}_\mathrm{R}$ is given by

$$\big[\mathbf{A}_\mathrm{R}\big]=\begin{bmatrix}a_1^2 & a_1a_2 & 0\\ a_1a_2 & a_2^2 & 0\\ 0 & 0 & 0\end{bmatrix}. \tag{63}$$

Next, two further assumptions are made: (1) The complete incompressibility (i.e. $J=1$) is assumed for the analytical solution, and (2) no fluid is present (i.e. $\phi=1$). Under these assumptions, the Cauchy stress in (41) is now given by

$$\mathbf{T}=(1-f_\mathrm{R})(G\mathbf{B}-P\mathbf{1})+2f_\mathrm{R}E(I_4-1)(\mathbf{F}\mathbf{A}_\mathrm{R}\mathbf{F}^\top) \tag{64}$$

with

$$\left.\begin{aligned} G &= \frac{1}{3}G_0\left(\frac{3-(\bar{\lambda}/\lambda_L)^2}{1-(\bar{\lambda}/\lambda_L)^2}\right)\text{ and}\\ I_4 &= a_1^2+2a_1a_2\gamma+(1+\gamma^2)a_2^2. \end{aligned}\right\} \tag{65}$$

Note that P in (64) denotes a constitutively indeterminate pressure, which is introduced to satisfy the incompressibility constraint.

For material parameters, we again use the same parameters that are shown in Table 1 and a volume fraction $f_\mathrm{R}=0.5$ for the fibers. On the numerical side, to approximate a nearly incompressible material we take $K=10^3G_0$. Since we are interested in verifying the mechanical response in the presence of fibers, we take three independent cases, $\mathbf{a}_\mathrm{R}=[1,0,0]^\top$, $\mathbf{a}_\mathrm{R}=[1/\sqrt{2},1/\sqrt{2},0]^\top$, and $\mathbf{a}_\mathrm{R}=[0,1,0]^\top$, to investigate different initial fiber orientations.

Fig. 11 compares the analytical with a single element (U3D8) simulation for the shear stress and normal stress difference given by

$$T_{12}=(1-f_\mathrm{R})G\gamma+2f_\mathrm{R}E(I_4-1)(a_1a_2+a_2^2\gamma) \tag{66}$$

and,

$$\begin{aligned} T_{11}-T_{33} &= (1-f_\mathrm{R})G\gamma^2\\ &\quad +2f_\mathrm{R}E(I_4-1)(a_1^2+2a_1a_2\gamma+a_2^2\gamma^2) \end{aligned} \tag{67}$$

respectively, against the numerical solutions. We note that the stress is normalized by the initial shear modulus G_0, and the cases $\mathbf{a}_\mathrm{R}=[1,0,0]^\top$, $\mathbf{a}_\mathrm{R}=[1/\sqrt{2},1/\sqrt{2},0]^\top$, and $\mathbf{a}_\mathrm{R}=[0,1,0]^\top$, are shown in Fig. 11b, c and d, respectively. The solid and dashed lines represent the analytical solutions, and the markers the numerically calculated results. It is worth mentioning that the case with the referential fiber orientation of $\mathbf{a}_\mathrm{R}=[1,0,0]^\top$ does not involve stretching along the fiber direction, which makes the model exhibit a pure hyperelastic response. Finally, the good agreement between analytical and numerical results indicate the mechanical portion including fibers of our finite element implementation is verified.

Supplementary material

Supplementary material associated with this article can be found, in the online version, at 10.1016/j.mechrescom.2019.02.002.

References

[1] Abaqus/Standard, Abaqus Reference Manuals, Dassault Systemes Simulia, Providence, RI, 2018.
[2] M. Agoras, O. Lopez-Pamies, P.P. Castañeda, A general hyperelastic model for incompressible fiber-reinforced elastomers, J. Mech. Phys. Solids 57 (2) (2009) 268–286.
[3] L. Anand, A constitutive model for compressible elastomeric solids, Comput. Mech. 18 (5) (1996) 339–355.
[4] E.M. Arruda, M.C. Boyce, A three-dimensional constitutive model for the large stretch behavior of rubber elastic materials, J. Mech. Phys. Solids 41 (2) (1993) 389–412.
[5] S. Baek, A. Srinivasa, Diffusion of a fluid through an elastic solid undergoing large deformation, Int. J. Non Linear Mech. 39 (2) (2004) 201–218.
[6] R. Bhavsar, N.Y. Vaidya, P. Ganguly, A. Humphreys, A. Robisson, H. Tu, N. Wicks, G.H. McKinley, F. Pauchet, Intelligence in novel materials, Oilfield Rev. 20 (1) (2008) 32–41.
[7] J.C. Breger, C. Yoon, R. Xiao, H.R. Kwag, M.O. Wang, J.P. Fisher, T.D. Nguyen, D.H. Gracias, Self-folding thermo-magnetically responsive soft microgrippers, ACS Appl. Mater. Interfaces 7 (5) (2015) 3398–3405.
[8] S. Cantournet, M. Boyce, A. Tsou, Micromechanics and macromechanics of carbon nanotube-enhanced elastomers, J. Mech. Phys. Solids 55 (6) (2007) 1321–1339.
[9] V. Chan, K. Park, M.B. Collens, H. Kong, T.A. Saif, R. Bashir, Development of miniaturized walking biological machines, Sci. Rep. 2 (2012) 857.
[10] S. Chaterji, I.K. Kwon, K. Park, Smart polymeric gels: redefining the limits of biomedical devices, Prog. Polym. Sci. 32 (8–9) (2007) 1083–1122.
[11] S.A. Chester, A constitutive model for coupled fluid permeation and large viscoelastic deformation in polymeric gels, Soft Matter 8 (31) (2012) 8223–8233.
[12] S.A. Chester, L. Anand, A coupled theory of fluid permeation and large deformations for elastomeric materials, J. Mech. Phys. Solids 58 (11) (2010) 1879–1906.
[13] S.A. Chester, L. Anand, A thermo-mechanically coupled theory for fluid permeation in elastomeric materials: application to thermally responsive gels, J. Mech. Phys. Solids 59 (10) (2011) 1978–2006.
[14] S.A. Chester, C.V. Di Leo, L. Anand, A finite element implementation of a coupled diffusion-deformation theory for elastomeric gels, Int. J. Solids Struct. 52 (2015) 1–18.
[15] B. Coudrillier, J. Tian, S. Alexander, K.M. Myers, H.A. Quigley, T.D. Nguyen, Biomechanics of the human posterior sclera: age-and glaucoma-related changes measured using inflation testing, Invest. Ophthalmol. Visual Sci. 53 (4) (2012) 1714–1728.
[16] B. Coudrillier, C. Boote, H.A. Quigley, T.D. Nguyen, Scleral anisotropy and its effects on the mechanical response of the optic nerve head, Biomech. Model. Mechanobiol. 12 (5) (2013) 941–963.
[17] E. de Souza Neto, D. Perić, M. Dutko, D. Owen, Design of simple low order finite elements for large strain analysis of nearly incompressible solids, Int. J. Solids Struct. 33 (20–22) (1996) 3277–3296.
[18] M. Doi, Gel dynamics, J. Phys. Soc. Jpn. 78 (5) (2009). 052001–052001
[19] F.P. Duda, A.C. Souza, E. Fried, A theory for species migration in a finitely strained solid with application to polymer network swelling, J. Mech. Phys. Solids 58 (4) (2010) 515–529.
[20] C. Durning, K. Morman Jr, Nonlinear swelling of polymer gels, J. Chem. Phys. 98 (5) (1993) 4275–4293.
[21] P.J. Flory, Thermodynamics of high polymer solutions, J. Chem. Phys. 10 (1) (1942) 51–61.
[22] R. Fuhrer, E.K. Athanassiou, N.A. Luechinger, W.J. Stark, Crosslinking metal nanoparticles into the polymer backbone of hydrogels enables preparation of soft, magnetic field-driven actuators with muscle-like flexibility, Small 5 (3) (2009) 383–388.
[23] Q. Ge, H.J. Qi, M.L. Dunn, Active materials by four-dimension printing, Appl. Phys. Lett. 103 (13) (2013) 131901.
[24] X. Gong, K. Yang, J. Xie, Y. Wang, P. Kulkarni, A.S. Hobbs, A.D. Mazzeo, Rotary actuators based on pneumatically driven elastomeric structures, Adv. Mater. 28 (34) (2016) 7533–7538.
[25] M.E. Gurtin, E. Fried, L. Anand, The Mechanics and Thermodynamics of Continua, Cambridge University Press, 2010.
[26] D. Han, C. Farino, C. Yang, T. Scott, D. Browe, W. Choi, J.W. Freeman, H. Lee, Soft robotic manipulation and locomotion with a 3d printed electroactive hydrogel, ACS Appl. Mater. Interfaces (2018).
[27] D. Han, Z. Lu, S.A. Chester, H. Lee, Micro 3d printing of a temperature-responsive hydrogel using projection micro-stereolithography, Sci. Rep. 8 (1) (2018) 1963.
[28] G.A. Holzapfel, Nonlinear Solid Mechanics: A Continuum Approach for Engineering, Wiley, 2000.
[29] G.A. Holzapfel, T.C. Gasser, A viscoelastic model for fiber-reinforced composites at finite strains: continuum basis, computational aspects and applications, Comput. Methods Appl. Mech. Eng. 190 (34) (2001) 4379–4403.
[30] W. Hong, X. Zhao, J. Zhou, Z. Suo, A theory of coupled diffusion and large deformation in polymeric gels, J. Mech. Phys. Solids 56 (5) (2008) 1779–1793.
[31] M.L. Huggins, Some properties of solutions of long-chain compounds, J. Phys. Chem. 46 (1) (1942) 151–158.
[32] F. Ilievski, A.D. Mazzeo, R.F. Shepherd, X. Chen, G.M. Whitesides, Soft robotics for chemists, Angewandte Chemie 123 (8) (2011) 1930–1935.
[33] M. Jamal, S.S. Kadam, R. Xiao, F. Jivan, T.-M. Onn, R. Fernandes, T.D. Nguyen, D.H. Gracias, Bio-origami hydrogel scaffolds composed of photocrosslinked peg bilayers, Adv. Healthc. Mater. 2 (8) (2013) 1142–1150.
[34] M. Kleverlaan, R.H. van Noort, I. Jones, et al., Deployment of swelling elastomer packers in shell e&p, in: SPE/IADC Drilling Conference, Society of Petroleum Engineers, 2005.
[35] C.K. Kuo, P.X. Ma, Ionically crosslinked alginate hydrogels as scaffolds for tissue engineering: part 1. structure, gelation rate and mechanical properties, Biomaterials 22 (6) (2001) 511–521.
[36] H. Li, G. Go, S.Y. Ko, J.-O. Park, S. Park, Magnetic actuated ph-responsive hydrogel-based soft micro-robot for targeted drug delivery, Smart Mater. Struct. 25 (2) (2016) 027001.
[37] M. Liu, X. Zeng, C. Ma, H. Yi, Z. Ali, X. Mou, S. Li, Y. Deng, N. He, Injectable hydrogels for cartilage and bone tissue engineering, Bone Res. 5 (2017) 17014.
[38] A. Lucantonio, P. Nardinocchi, L. Teresi, Transient analysis of swelling-induced large deformations in polymer gels, J. Mech. Phys. Solids 61 (1) (2013) 205–218.
[39] A. Lucantonio, L. Teresi, A. DeSimone, Continuum theory of swelling material surfaces with applications to thermo-responsive gel membranes and surface mass transport, J. Mech. Phys. Solids 89 (2016) 96–109.
[40] P. Nardinocchi, M. Pezzulla, L. Teresi, Anisotropic swelling of thin gel sheets, Soft Matter 11 (8) (2015) 1492–1499.
[41] P. Nardinocchi, L. Teresi, Actuation performances of anisotropic gels, J. Appl. Phys. 120 (21) (2016) 215107.
[42] T. Nguyen, R. Jones, B. Boyce, A nonlinear anisotropic viscoelastic model for the tensile behavior of the corneal stroma, J. Biomech. Eng. 130 (4) (2008) 041020.
[43] T.D. Nguyen, R. Jones, B. Boyce, Modeling the anisotropic finite-deformation viscoelastic behavior of soft fiber-reinforced composites, Int. J. Solids Struct. 44 (25–26) (2007) 8366–8389.
[44] M. Otake, Y. Kagami, M. Inaba, H. Inoue, Motion design of a starfish-shaped gel robot made of electro-active polymer gel, Rob. Auton. Syst. 40 (2–3) (2002) 185–191.
[45] Y. Pan, Z. Zhong, A nonlinear constitutive model of unidirectional natural fiber reinforced composites considering moisture absorption, J. Mech. Phys. Solids 69 (2014) 132–142.
[46] J.K. Pijanka, B. Coudrillier, K. Ziegler, T. Sorensen, K.M. Meek, T.D. Nguyen, H.A. Quigley, C. Boote, Quantitative mapping of collagen fiber orientation in non-glaucoma and glaucoma posterior human sclerae, Invest. Ophthalmol. Visual Sci. 53 (9) (2012) 5258–5270.
[47] J. Ryu, M. D'Amato, X. Cui, K.N. Long, H. Jerry Qi, M.L. Dunn, Photo-origami — bending and folding polymers with light, Appl. Phys. Lett. 100 (16) (2012) 161908.
[48] T. Tanaka, D.J. Fillmore, Kinetics of swelling of gels, J. Chem. Phys. 70 (3) (1979) 1214–1218.
[49] M. Wehner, R.L. Truby, D.J. Fitzgerald, B. Mosadegh, G.M. Whitesides, J.A. Lewis, R.J. Wood, An integrated design and fabrication strategy for entirely soft, autonomous robots, Nature 536 (7617) (2016) 451.
[50] J.A. Weiss, B.N. Maker, S. Govindjee, Finite element implementation of incompressible, transversely isotropic hyperelasticity, Comput. Methods Appl. Mech. Eng. 135 (1–2) (1996) 107–128.
[51] J. Xie, J.B. McGovern, R. Patel, W. Kim, S. Dutt, A.D. Mazzeo, Elastomeric actuators on airfoils for aerodynamic control of lift and drag, Adv. Eng. Mater. 17 (7) (2015) 951–960.
[52] Z. Zhao, X. Kuang, J. Wu, Q. Zhang, G.H. Paulino, H.J. Qi, D. Fang, 3d printing of complex origami assemblages for reconfigurable structures, Soft Matter 14 (39) (2018) 8051–8059.
[53] W.J. Zheng, N. An, J.H. Yang, J. Zhou, Y.M. Chen, Tough al-alginate/poly (n-isopropylacrylamide) hydrogel with tunable lcst for soft robotics, ACS Appl. Mater. Interfaces 7 (3) (2015) 1758–1764.